Quasielastic scattering of light radioactive and stable projectiles on ^{9}Be

U. Umbelino,* R. Lichtenthäler,† O. C. B. Santos, K. C. C. Pires, A. S. Serra, V. Scarduelli, A. L. de Lara, E. O. N. Zevallos, J. C. Zamora, and A. Lépine-Szily
Instituto de Física, Universidade de São Paulo, São Paulo 05508-090, São Paulo, Brazil

J. M. B. Shorto
Instituto de Pesquisas Energéticas e Nucleares (IPEN-CNEN), São Paulo 05508-000, São Paulo, Brazil

M. Assunção
Departamento de Física, Universidade Federal de São Paulo, Campus Diadema, São Paulo 09913-030, São Paulo, Brazil

V. A. B. Zagatto
Instituto de Física, Universidade Federal Fluminense, Niterói 24210-340, Rio de Janeiro, Brazil

(Received 9 September 2022; accepted 13 October 2022; published 2 November 2022)

Quasielastic scattering angular distributions of radioactive (^{8}Li, ^{7,10}Be, and ^{8,12}B) and stable (^{6,7}Li, ^{9}Be, and ^{11}B) projectiles on a ^{9}Be target are presented. The angular distributions have been analyzed by the optical model using Woods-Saxon form factor and São Paulo potential. Total reaction cross sections have been obtained from the optical model analysis and a comparison between different systems is presented. Coupled channels (CC), coupled reaction channels (CRC), and continuum-discretized coupled channels (CDCC) calculations have been performed to investigate the effect of the cluster configuration in the projectile inelastic excitation, breakup, and stripping reactions on the quasielastic angular distributions.

DOI: 10.1103/PhysRevC.106.054602

I. INTRODUCTION

Low energy scattering experiments induced by weakly bound stable and unstable projectiles have been performed in recent years [1–9]. Many experiments combine the incidence of light projectiles on intermediate or heavy mass targets [10–13] in situations where the ratio between the beam energy and the Coulomb barrier is not too large ($E/V_B \approx$ 1–2), while experimental data with light targets is still very scarce [2,3,5]. For collisions induced by exotic neutron halo projectiles such as ^{6}He, ^{11}Li, and ^{11}Be on intermediate and heavy mass targets such as ^{64}Zn, ^{120}Sn, ^{208}Pb, and ^{209}Bi, a strong suppression of the Fresnel peak has been observed, in comparison to stable systems [6,13–18]. This suppression is a well known phenomenon, due to the coupling between the elastic scattering with the projectile breakup channel. However, this effect has not been observed in the scattering of the proton-rich (p-rich) halo ^{8}B nucleus on intermediate ^{58}Zn [19] and heavy ^{208}Pb [20] mass targets.

For light mass systems, the decrease in the relative importance of the Coulomb repulsion ($E/V_B > 2$) changes the situation. As the ratio E/V_b increases, the Fresnel peak shifts to forward angles and the elastic cross section quickly decreases, with the onset of oscillations. This pattern can be understood as the result of an interference phenomena between two scattering amplitudes: the near-side amplitude corresponds to a trajectory that emerges on the same side of the scattering axis from where it has entered, and the far-side amplitude emerges from the opposite side [21]. At low E/V_b ratios, the first component dominates the angular distribution (Fresnel regime); as the energy increases the magnitude of the far-side component is enhanced and starts to significantly interfere with the near-side component. The period of the resulting oscillations is related to the grazing angular momentum of the collision ($\Delta\theta = \pi/l_g$), and a transition from Fresnel to Fraunhofer regimes takes place. The magnitude of the Sommerfeld parameter ($\eta = Z_1Z_2e^2/\hbar v$) gives an idea of the dominant regime, being $\eta \gg 1$ for Fresnel and $\eta \approx 1$ for Fraunhofer diffractions.

Usually, the total reaction cross sections are enhanced from strongly bound (^{4}He) to weakly bound (^{6,7}Li, ^{9}Be) and to exotic projectiles (^{6}He) on similar mass targets. For intermediate mass and heavy targets, researchers have already observed an enhancement of the total reaction cross sections of exotic systems when compared with stable tightly bound systems [10,22–25]. For lighter targets, understanding the importance of each reaction channel on the total reaction cross section still requires more experimental data [2,3,5].

In this paper we present new data of quasielastic scattering induced by stable and radioactive projectiles ^{6,7,8}Li, ^{7,9,10}Be, and ^{8,11,12}B on a ^{9}Be target. In Sec. II, we described the experimental setup. In Sec. III, we analyze the angular distributions

*uiran@if.usp.br
†rubens@if.usp.br

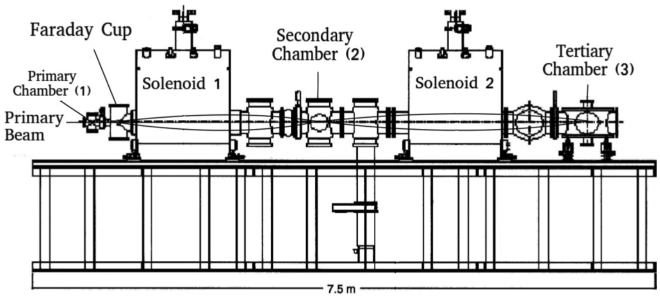

FIG. 1. RIBRAS scheme.

TABLE I. Average secondary beam intensities and the FWHM of the peaks (see text for more details).

Experiment	Projectile	Intensity (pps)	FWHM (MeV)
	^{6}Li	2.5×10^{3}	0.905
	^{7}Li	1.6×10^{4}	0.878
	^{8}Li	1.8×10^{3}	0.751
	^{9}Be	2.1×10^{4}	1.230
	^{10}Be	3.0×10^{4}	1.031
	^{11}B	1.2×10^{4}	1.423
^{10}Be + ^{9}Be	^{12}B	2.2×10^{4}	1.244
	^{6}Li	2.8×10^{6}	1.903
	^{7}Be	2.8×10^{4}	1.874
^{8}B + ^{9}Be	^{8}B	4.0×10^{3}	1.683

with optical model calculations, with a discussion for each system. In Sec. IV, we present a systematic analysis of the total reaction cross section. In Sec. V, the results of coupled channels (CC), continuum-discretized coupled channels (CDCC), and coupled reaction channels (CRC) are presented. Finally, in Sec. VI we draw our conclusions.

II. EXPERIMENTAL SETUP

Two experimental campaigns were performed in the secondary chamber (2) of the RIBRAS system (Radioactive Ion Beams in Brasil; see Fig. 1) [16,26–28] at the Nuclear Physics Open Laboratory of the Institute of Physics of the University of São Paulo. In the first experiment, ^{11}B primary beams at 34 and 38 MeV are provided by the 8-UD Pelletron accelerator and impinged on a beryllium production foil (2.59 mg/cm^2) located in the primary chamber (1). A secondary cocktail beam was produced with ^{6,7,8}Li, ^{9,10}Be, and ^{11,12}B isotopes. In the second experiment, a 32 MeV ^{6}Li primary beam and a ^{3}He gas primary target were used to produce ^{7}Be and ^{8}B secondary beams, in addition to the scattered ^{6}Li. The gaseous target consists of a 3.6 cm long cell sealed by two 2.04(2) μm Havar foils, kept at 1014 mbar pressure at room temperature.

The magnetic field of the first solenoid, located after the primary chamber, was adjusted (through current variation) to maximize the ^{10}Be and ^{8}B beams in the center of the ISO-250 secondary chamber (2). A ^{9}Be foil with 1.92 mg/cm^2 thickness was mounted as a secondary target in the center of the scattering chamber (2). An additional ^{197}Au (4.5 mg/cm^2) foil was used to monitor the secondary beam intensities and provide the cross section normalization. The secondary beam intensities were obtained by measuring the scattered beam on a gold target, and its average value is given in Table I for each experiment. The full widths at half maximum (FWHM) presented in Table I are related to the peak energy resolutions measured in the spectra of the present work and will be discussed later.

During the ^{10}Be + ^{9}Be experiments two silicon surface barrier telescopes detectors, with 25 μm (ΔE) and 1000 μm (E) thickness, were mounted in the scattering chamber to provide an energy measurement and particle identification in the angular range $12^\circ \leqslant \theta_{\rm lab} \leqslant 40^\circ$. A set of 3×12 mm rectangular collimators were used a distances of 6.3 and 8.2 cm from the target resulting in a 1.3° geometric angular aperture and an approximate 5 msr detection solid angle. Figure 2 presents two ΔE-$E_{\rm Total}$ spectra measured at 12° with gold (a) and beryllium (b) targets for the first experiment.

In both ^{10}Be + ^{9}Be experiments, the ΔE energy resolution allows the separation of all particles. The mass (m) and charge state (q) identification was done by imposing that they must have same magnetic rigidity [$(B\rho)^2 = 2mE/q^2$] after the solenoid selection, where E is the measured energy corrected by the energy loss in the secondary target. Figure 3 shows a $(B\rho)^2$ plot as a function of a generic peak number. We see from this figure that any misidentification of mass-charge ratio (m/q^2) or nuclear number would produce incompatible values

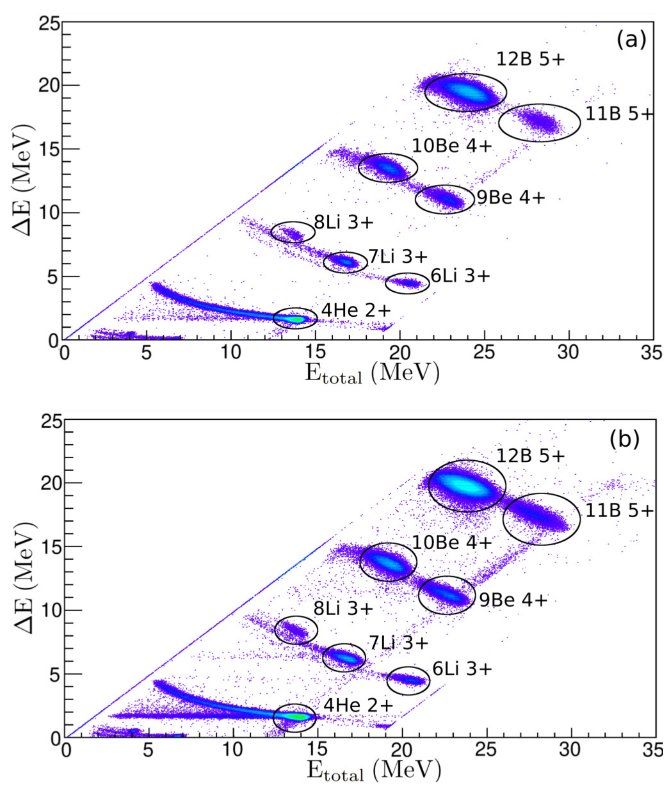

FIG. 2. ΔE-$E_{\rm Total}$ spectra of the cocktail beam produced in the ^{11}B + ^{9}Be reaction at $E_{^{11}\rm B} = 34$ MeV scattered on gold (a) and ^{9}Be (b) targets at $\theta_{\rm lab} = 12^\circ$.

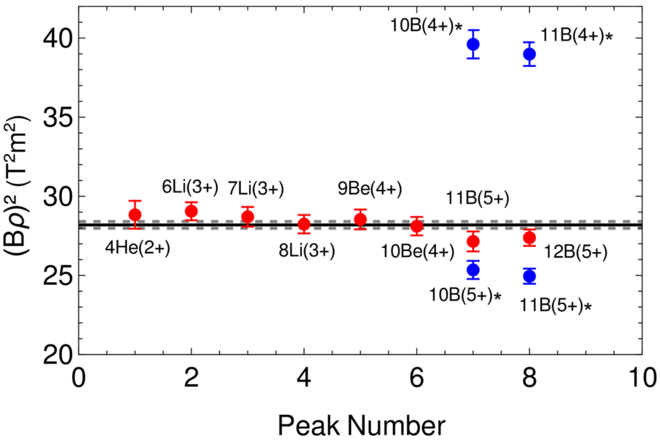

FIG. 3. Full identification of the cocktail beam by magnetic rigidity $(B\rho)^2$; the full and dashed lines shows the mean and deviation of $(B\rho)^2$.

of $(B\rho)^2$ (blue points), as observed in all wrong combinations for different boron isotopes (peaks number 7 and 8).

For the $^8\mathrm{B} + {}^9\mathrm{Be}$ experiment, only one silicon surface telescope detector with 20 μm (ΔE) and 1000 μm (E) thickness was mounted to observe the elastic scattering at forward angles. As in the ^{10}Be experiments, a pair of 3×12 mm rectangular collimators were used. Figure 4 shows the ΔE-E_{Total} spectra for the gold (a) and beryllium (b) targets for the second experiment. As one can observe, in this case the

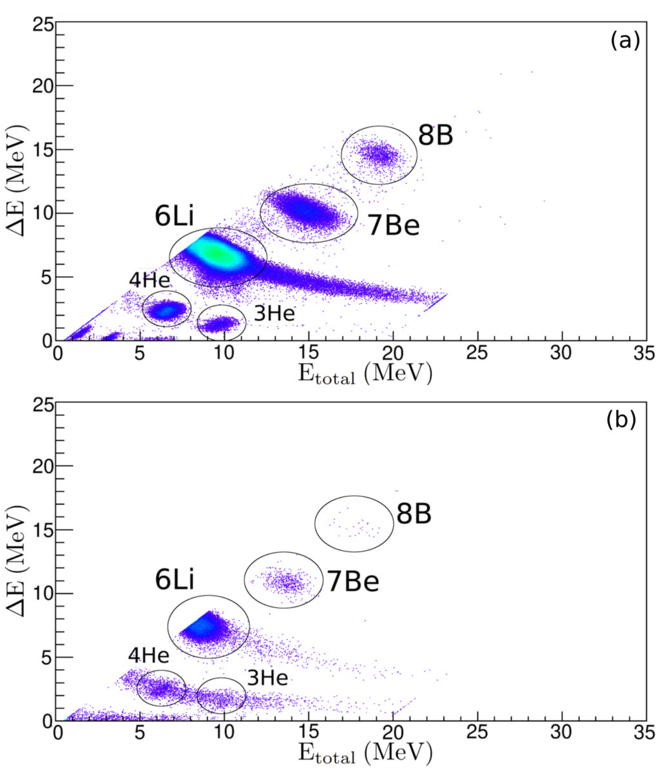

FIG. 4. ΔE-E_{Total} identification spectra of the cocktail beam produced in the $^6\mathrm{Li} + {}^3\mathrm{He}$ reaction at $E_{^6\mathrm{Li}} = 32$ MeV scattered on gold (a) and ^{9}Be (b) targets at $\theta_{\mathrm{lab}} = 12^\circ$.

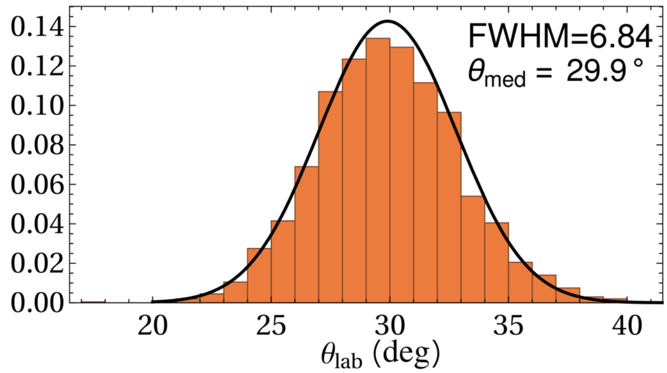

FIG. 5. Monte Carlo simulation of the distribution of scattering angles reaching one detector. The solid line is a Gaussian fit.

identification of the mass (m) and charge state (q) of the peaks was unambiguous, because there is only one peak for each interest atomic number (^{6}Li, ^{7}Be, and ^{8}B).

The energy resolution of the secondary beams produced at RIBRAS is determined mainly by two factors. The first is the energy straggling in the primary target, which is given by the difference between the outgoing projectile energies produced in the beginning and the end of the primary target. This is a significant factor for transfer reactions involving charge transfer (≈62%–84%). The second contribution stems from the kinematic broadening in the angular acceptance of the first solenoid (≈12%–35%). In addition to these two factors, the final energy resolution has a small contribution from the processes taking place in the secondary target, such as the kinematic broadening due to the angular acceptance of the detectors and the contribution from the electronic noise and detector resolution. This value was measured directly from the peak width (FWHM) using the gold target and is presented in Table I, together with the secondary beam intensities. In some cases such as ^{7,8}Li, ^{7}Be, and ^{12}B the energy resolution is not sufficient to separate the ground state and the low lying excited states. Therefore, the elastic peaks are possibly contaminated with counts from the inelastic scattering. In order to estimate this effect, we performed coupled channel calculations, which showed that this contribution would be negligible. These results will be presented and discussed in detail in Sec. V.

The angular resolution is mainly determined by three factors: the aperture of the telescope collimators, the beam spot size, and the angular divergence of the RIBRAS secondary beam. The latter is defined by the combined effect of angular acceptance (2°–6°) and magnification of the first solenoid, resulting in an intrinsic angular divergence of the secondary beam between 1.3°–4.0° in the center of the secondary scattering chamber. A three-dimensional Monte Carlo simulation [29] was performed to estimate the effective angular acceptance of the detectors, taking into account the beam divergence, the geometry of the collimators, the beam spot size and the angular straggling in the secondary target. As a result of this simulation (see Fig. 5), a distribution of scattering angles actually accepted by the detector was obtained as $\delta\theta_{\mathrm{lab}} \approx 2.9^\circ$ (FWHM $= 2.355 \times \delta\theta_{\mathrm{lab}}$). For almost symmetric

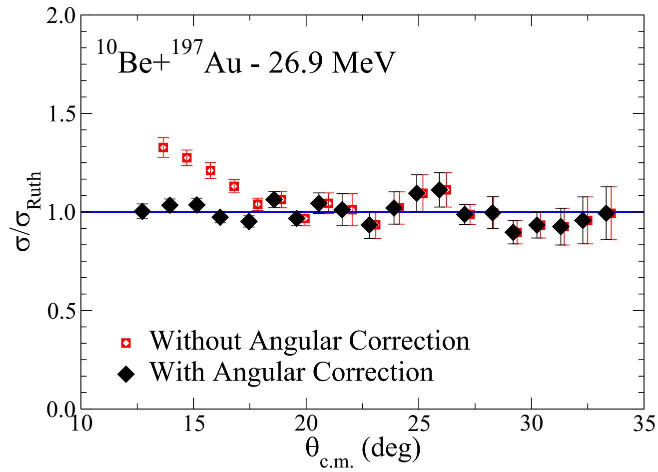

FIG. 6. Angular correction for the $^{10}\mathrm{Be} + {}^{197}\mathrm{Au}$ system.

systems, as in the present case, the kinematic angular transformation to the center-of-mass (CM) system is rather large, which makes the angular resolution in the CM system almost double that of the laboratory system ($\theta_{\mathrm{CM}} \sim 2\theta_{\mathrm{lab}}$). As a consequence, a smoothing effect in the amplitude of oscillatory angular distributions will take place. This effect was properly taken into account before comparing the calculations with the data, as described in the next section.

To monitor the secondary beam intensities and to obtain the normalized absolute cross sections, runs with ^{197}Au target were performed periodically before and after each ^{9}Be run. The elastic cross section on the gold target, at the energies and angles of these experiments, is pure Rutherford scattering and, due to this fact, provides an absolute normalization of the experimental cross sections, which is calculated by the following expression:

$$\frac{d\sigma}{d\Omega}_i = \frac{N_c^i J^i}{N_b^i N_t^i \Delta\Omega} \tag{1}$$

where the index i refers to each secondary target ($i = \mathrm{Au}$ or $i = \mathrm{Be}$), N_c^i is number of events in the peak, J^i is the Jacobian transformation factor between the laboratory and center-of-mass frameworks, N_t^i is the areal density of particles in the target, N_b^i is the number of incident secondary beam particles, and $\Delta\Omega$ is the solid angle of the detection system.

Figure 6 shows the $\sigma/\sigma_{\mathrm{Ruth}}$ ratio for $^{10}\mathrm{Be} + {}^{197}\mathrm{Au}$ measured at 26.9 MeV calculated using Eq. (1) (red dots). We see that, for large angles, the $\sigma/\sigma_{\mathrm{Ruth}}$ ratio is constant around unity. However, for angles below 20°, the ratio starts to increase to values larger than 1, indicating that some spurious effect is taking place at very forward angles. The reason for that is the large angular acceptance associated with the rapid decrease of the Rutherford cross section, which increases the peak counts with frontal events. This effect shifts the average detection angle to forward, with respect to the nominal geometric central angle of the detector. This shift can be obtained by the Monte Carlo simulation, for each angle, and the corrected values are presented in Fig. 6 (black points).

The absolute normalized scattering cross sections for the ^{9}Be target are

$$\frac{d\sigma}{d\Omega}_{\mathrm{Be}} = \frac{d\sigma}{d\Omega}^{\mathrm{Ruth}}_{\mathrm{Au}} \times \left[\frac{N_c^{\mathrm{Be}}}{N_c^{\mathrm{Au}}} \frac{J^{\mathrm{Be}}}{J^{\mathrm{Au}}} \frac{N_t^{\mathrm{Au}}}{N_t^{\mathrm{Be}}} \frac{N_b^{\mathrm{Au}}}{N_b^{\mathrm{Be}}}\right], \tag{2}$$

where $\frac{N_b^{\mathrm{Au}}}{N_b^{\mathrm{Be}}}$ is taken to be equal to the ratio of the primary beam integration, measured by a Faraday cup in the corresponding runs (see Fig. 1), and $\frac{J^{Be}}{J^{Au}}$ is the ratio of the Jacobians for beryllium and gold targets as defined in Eq. (1). The solid angle dependence cancels out in the above expression because it is a pure geometric quantity not depending on the secondary target element used. This quantity cannot be easily determined given its dependence with the beam spot size, divergence, collimators, and detector geometry. The experimental uncertainties were taken to be the statistical errors ($\sqrt{N}$) plus a small contribution due to the error in the target thickness, which was estimated as 5%.

III. ANALYSIS OF THE ANGULAR DISTRIBUTIONS

In this section, the angular distributions and the results of optical model calculations for all projectiles on the ^{9}Be target are presented. The theoretical analysis were performed using the code FRESCO [30]. We used complex volumetric potentials combined with two different shapes: a Woods-Saxon (WS) potential and the double folding São Paulo potential [31]. The usual WS form factor is given by

$$f_i(r) = -\frac{1}{1 + \exp\left[\frac{r - R_i}{a_i}\right]}, \tag{3}$$

where the index i stands for the real and imaginary components, $R_i = r_0(A_p^{1/3} + A_t^{1/3})$ being the interaction radius and a_i the nuclear diffuseness. The values initially used here for the reduced radius and the nuclear diffuseness are, respectively, $r_0 = 1.25$ fm and $a_i = 0.65$ fm. The complex optical potential are formed by the WS form factor as $V_{\mathrm{opt}}^{\mathrm{WS}} = V f_{\mathrm{Re}} + iW f_{\mathrm{Im}}$, where V and W are the real and imaginary depths, respectively.

The double folding São Paulo potential (SPP1) has the same form factor (f_{SPP}) for the real and imaginary components with different normalization values. The final complex São Paulo potential is given as $V_{\mathrm{opt}}^{\mathrm{SPP}} = (N_{\mathrm{Re}} + iN_{\mathrm{Im}})f_{\mathrm{SPP}}$, where the standard normalization [32] values ($N_{\mathrm{Re}} = 1$ and $N_{\mathrm{Im}} = 0.78$) were used in the present work, initially, for all systems. Eventually, to better reproduce the data, the real and imaginary normalizations were varied with a routine that will be described latter in this section. We also used the new version of the São Paulo potential (SPP2) [33], which includes realistic information about nuclear density of stable isotopes or away from the stability valley. The values of the real and imaginary normalizations were varied to best fit the data.

As mentioned in the experimental section, due to the large angular acceptance involved in these measurements, all the theoretical angular distributions were folded with a Gaussian distribution centered in the scattering angle (θ'), with standard deviation equal to the experimental angular acceptance

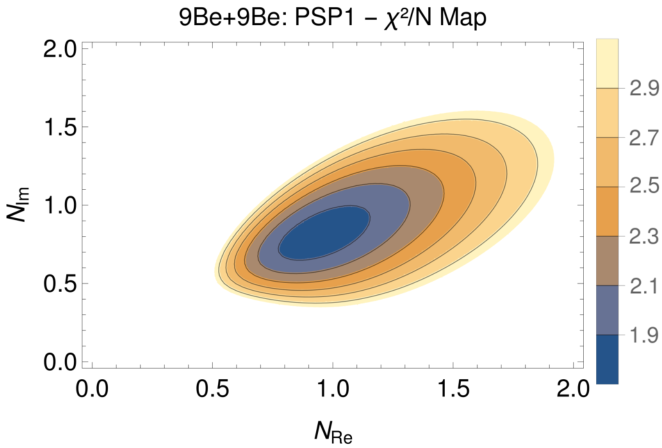

FIG. 7. χ^2/N map of the ^{9}Be + ^{9}Be system at 24.3 MeV and 30.1 MeV (Fig. 13).

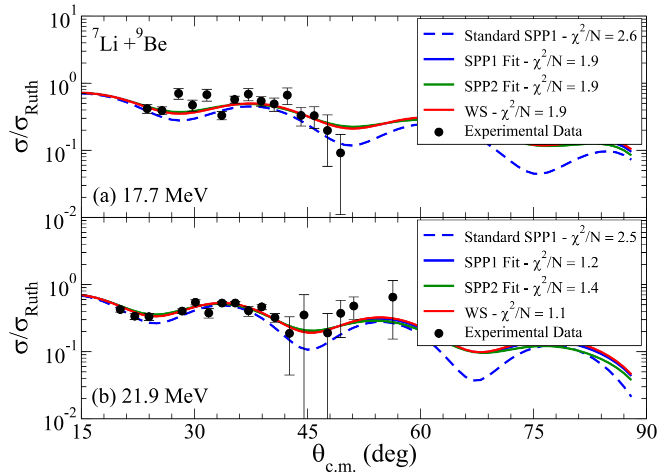

FIG. 9. Angular distributions of the ^{7}Li + ^{9}Be system at E_{lab} = 17.7 (a) and 21.9 MeV (b) compared with theoretical results.

$(\delta\theta_{\mathrm{CM}})$:

$$\left(\frac{d\sigma}{d\Omega}\right)_{\mathrm{conv}} = \int_{\theta'-\pi}^{\theta'+\pi} \left(\frac{d\sigma}{d\Omega}\right)_{\mathrm{theo}} \frac{1}{\delta\theta_{\mathrm{CM}}\sqrt{2\pi}} e^{-\frac{(\theta-\theta')^2}{2\delta\theta_{\mathrm{CM}}^2}} d\theta \quad (4)$$

The effect of this folding is to slightly reduce the amplitude of the oscillations in the angular distributions.

We use an automatic search method to find the best parameters. Initially, the Woods-Saxon depths (V and W) or São Paulo potential normalizations (N_{Re} and N_{Im}) were varied in a grid. A routine was written to set initial parameters and grid definitions (range and step), run the optical model to obtain the theoretical cross sections, perform the angular convolution as described above and calculate the chi-squared values in the grid. Then, the program *Mathematica* [34] is called to interpolate and find the minimum in the grid. The uncertainties were obtained as the width of the map when the total χ^2 is increased by one unit around the minimum. Whenever necessary, a search in the Woods-Saxon geometry parameters (r_0, a_0, r_i, and a_i) was performed to improve the fit. The obtained χ^2 maps were compared for the same projectile and target combination at different energies and, if they presented nearby minima, a global χ^2/N plot was built to provide a unique potential. Figure 7 shows an example of a contour plot for the ^{9}Be + ^{9}Be system at two energies. The normalizations of the São Paulo potential were varied from 0 to 2 in a 0.025 steps. Detailed results for each system will be presented in the next subsections.

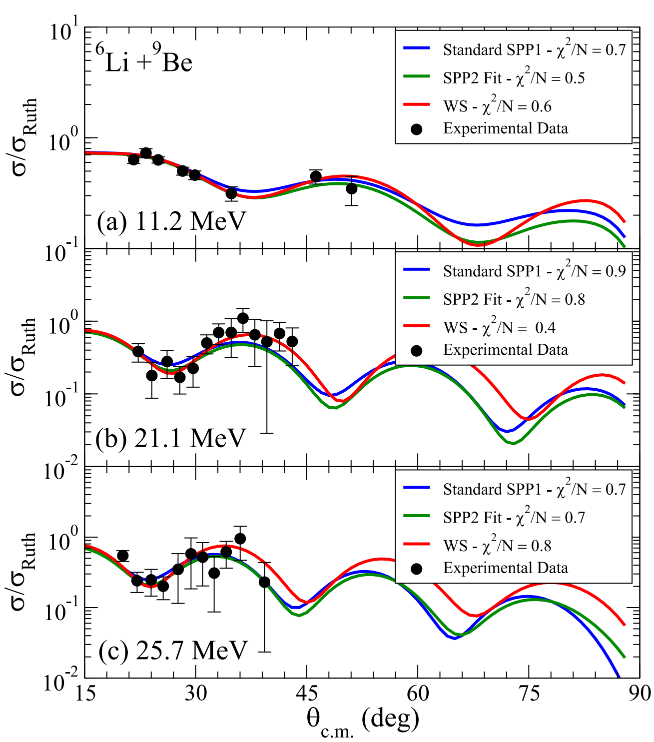

FIG. 8. Angular distributions of the ^{6}Li + ^{9}Be system at E_{lab} = 11.2 (a), 21.1 (b), and 25.7 MeV (c) compared with theoretical results.

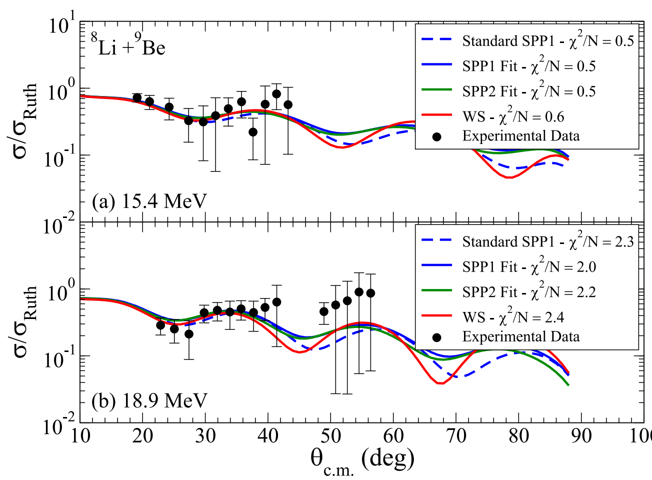

FIG. 10. Angular distributions of the ^{8}Li + ^{9}Be system at E_{lab} = 15.4 (a) and 18.9 MeV (b) compared with theoretical results.

TABLE II. Optical model parameters for the lithium systems, obtained by a systematic search (the parameters without uncertainties were kept fixed during the search). See the text for more details.

		Woods-Saxon							SPP1				SPP2		
Projectile	E_{lab} (MeV)	V (MeV)	r_0 (fm)	a_0 (fm)	W (MeV)	r_i (fm)	a_i (fm)	χ^2/N	N_{Re}	N_{Im}	χ^2/N Stand.	χ^2/N Varied	N_{Re}	N_{Im}	χ^2/N Varied
	11.2	12.2(2)	1.25	0.65	7.3(2)	1.25	0.65	0.6	1.0	0.78	0.7		0.58(2)	0.41(2)	0.5
	21.1	12.2(2)	1.25	0.65	7.3(2)	1.25	0.65	0.4	1.0	0.78	0.9		0.58(2)	0.41(2)	0.8
^{6}Li	25.7	12.2(2)	1.25	0.65	7.3(2)	1.25	0.65	0.8	1.0	0.78	0.7		0.58(2)	0.41(2)	0.7
	17.7	9.6(2)	1.25	0.65	15.4(3)	1.25	0.65	1.9	0.67(2)	1.07(2)	2.6	1.9	0.32(8)	0.67(1)	1.9
^{7}Li	21.9	9.6(2)	1.25	0.65	15.4(3)	1.25	0.65	1.1	0.67(2)	1.07(2)	2.5	1.2	0.32(8)	0.67(1)	1.4
	15.4	12.5(4)	1.25	0.65	4.8(1)	1.4(1)	0.8(1)	0.6	1.0(2)	1.2(3)	0.5	0.5	0.6(1)	0.8(1)	0.5
^{8}Li	18.9	15.8(5)	1.25	0.65	7.2(2)	1.25	0.9(1)	2.4	1.0(2)	1.2(3)	2.3	2.0	0.6(1)	0.8(1)	2.2

A. Lithium isotopes

The ^{6,7,8}Li elastic scattering on ^{9}Be was measured at $E_{\mathrm{lab}}^{^6\mathrm{Li}} = 11.2$, 21.1, and 25.7 MeV; $E_{\mathrm{lab}}^{^7\mathrm{Li}} = 17.7$ and 21.9 MeV; and $E_{\mathrm{lab}}^{^8\mathrm{Li}} = 15.4$ and 18.9 MeV. The Coulomb barriers are at $V_{\mathrm{b}}^{^6\mathrm{Li}} = 3.31$, $V_{\mathrm{b}}^{^7\mathrm{Li}} = 3.48$, and $V_{\mathrm{b}}^{^8\mathrm{Li}} = 3.64$ MeV [35] in the laboratory system. The results are presented in Figs. 8–10 and the final parameters in Table II.

All the experimental data of the ^{6}Li isotope were well reproduced by the same general potential: the geometric parameters used in the WS form factor were fixed in the standard values ($r_i = 1.25$ fm and $a_i = 0.65$ fm). Results using SPP1 with the standard normalization values ($N_{\mathrm{Re}} = 1$ and $N_{\mathrm{Im}} = 0.78$) are in good agreement with the data. For SPP2 a systematic reduction in the normalizations was obtained, where it is important to highlight the differences in nuclear densities and interaction form between the two versions of the São Paulo potentials that can cause these differences.

The ^{7}Li data are in reasonable agreement with the theoretical results of a general potential. For the WS potential, the geometric parameters does not need to be varied, imaginary depths are larger then the real counterparts. For SPP1 we observed that the standard normalizations provides a reasonable description of the elastic cross section, reproducing the oscillations. However, the search for parameters gives greater importance to points with smaller uncertainties in specific regions and, therefore, the validity of the standard normalizations cannot be discarded. Again, the SPP2 values are smaller than the SPP1 ones.

For the radioactive $^8\mathrm{Li} + {}^9\mathrm{Be}$ system, equal normalizations (SPP1 and SPP2) for both energies are obtained and slightly different WS potentials are needed. Compared with the real ones, larger imaginary geometric parameters and normalizations were obtained in all cases, showing the effect of the strong cluster configuration $^8\mathrm{Li} \rightarrow {}^7\mathrm{Li} + n$ ($S_n = 2.032$ MeV). This potential shape causes a strong absorption, that may increase the direct reaction channels' importance. Comparing the obtained potentials shapes, we can obtain interesting clues about the sensitivity radius of the real and imaginary parts. This plot can be observed in Fig. 11 for the lithium systems, where only one image will be presented for systems with global potentials. As can be observed, there are differences in the potential depths in the internal region ($r \leqslant 6$ fm), where SPPs are deeper than the WS one, and still lack more backward data to obtain information about the inner potentials. However, the ^{6,7}Li real and imaginary potentials converges in the peripheral region, resulting in almost identical cross sections in the angular range of the data (Igo's ambiguities [36]). For the ^{8}Li cases a long range imaginary potential was produced by a high nuclear diffuseness in the WS form factor, but not reproduced by SPPs.

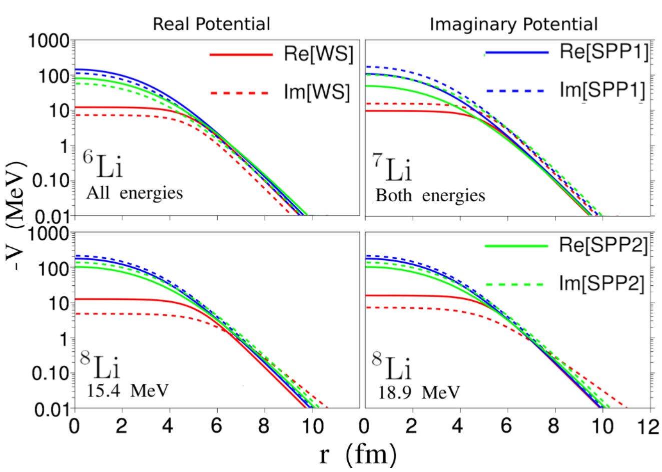

FIG. 11. Optical potentials obtained for lithium systems.

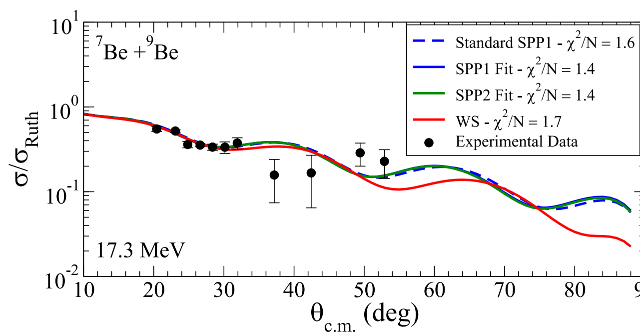

FIG. 12. Angular distribution of the $^7\mathrm{Be} + {}^9\mathrm{Be}$ system at $E_{\mathrm{lab}} = 17.3$ MeV compared with theoretical results.

TABLE III. Optical model parameters for the beryllium systems, obtained by a systematic search (the parameters without uncertainties were kept fixed during the search).

Projectile	E_{lab} (MeV)	Woods-Saxon V (MeV)	r_0 (fm)	a_0 (fm)	W (MeV)	r_i (fm)	a_i (fm)	χ^2/N	SPP1 N_{Re}	N_{Im}	χ^2/N Stand.	χ^2/N Varied	SPP2 N_{Re}	N_{Im}	χ^2/N Varied
^{7}Be	17.3	11.1(1)	1.25	0.65	7.0(1)	1.25	1.04(1)	1.7	1.14(1)	0.87(2)	1.6	1.4	0.69(4)	0.56(1)	1.4
	24.3	13.7(2)	1.25	0.65	12.7(2)	1.25	0.65	1.3	0.94(1)	0.80(1)	2.0	1.4	0.56(1)	0.53(1)	1.4
^{9}Be	30.1	13.7(2)	1.25	0.65	12.7(2)	1.25	0.65	2.8	0.94(1)	0.80(1)	2.0	2.0	0.56(1)	0.53(1)	2.0
	21.8	14.2(2)	1.25	0.65	10.6(2)	1.25	0.88(5)	2.4	2.07(4)	0.85(2)	4.6	2.5	1.33(2)	0.54(2)	2.6
^{10}Be	26.9	12.7(2)	1.25	0.65	12.1(2)	1.25	0.65	1.9	0.82(1)	0.81(1)	2.5	2.0	0.54(1)	0.56(1)	2.1

B. Beryllium isotopes

A $^7\text{Be} + {}^9\text{Be}$ angular distribution was measured at $E_{\text{lab}}^{^7\text{Be}} = 17.3$ MeV, well above the Coulomb barrier at $V_{\text{b}}^{^7\text{Be}} = 4.79$ MeV. The experimental data and optical model fits can be observed in Fig. 12, where one can observe that a reasonable fit is obtained with both versions of the São Paulo potential and a considerable improvement in the χ^2/N is obtained using a Woods-Saxon form factor with parameters given in Table III. There is noticeable large imaginary diffuseness of the WS potential due to the loosely bound $^7\text{Be} \rightarrow {}^4\text{He} + {}^3\text{He}$ ($S_\alpha = 1.587$ MeV) cluster configuration, in agreement with the results from Ref. [5].

Two angular distributions for the symmetric $^9\text{Be} + {}^9\text{Be}$ system at $E_{\text{lab}}^{^9\text{Be}} = 24.3$ and 30.1 MeV ($V_{\text{b}}^{^9\text{Be}} = 5.24$ MeV) are presented in Fig. 13 and the obtained parameters are in Table III. In all cases, the oscillations in the angular distributions are well reproduced by the same general potential. The standard SPP1 provides reasonable fits, with a slight variation to best reproduce the data, and smaller normalizations are required by SPP2. In the case of the WS analysis, a standard geometric shape was used in imaginary and real components.

For the $^{10}\text{Be} + {}^9\text{Be}$ scattering, two angular distributions were measured at $E_{\text{lab}}^{^{10}\text{Be}} = 21.8$ and 26.9 MeV ($V_{\text{b}}^{^{10}\text{Be}} = 5.47$ MeV). The results are presented in Fig. 14 and in Table III. The oscillations in the angular distributions are well reproduced by both São Paulo and Woods-Saxon potentials, with small variations around the standard geometries. A slight increase in the WS imaginary diffuseness seems to be necessary to improve the fit at lower energy, possibly indicating some increasing surface absorption for this neutron rich system. However, significant real normalizations (SPP) are also needed to reproduce the data. At higher energy, all potentials parameters indicate some equivalence by refraction and absorption.

The potentials plots for the beryllium systems can be observed in Fig. 15. Again, a clear difference is observed in the inner potential when WS and SPPs are compared. For the ^{7}Be, the WS form factor extends its imaginary potential to greater distances than the real counterpart, producing a strong absorption in this region. The ^{9}Be potentials show a remarkable consistency in the peripheral region, producing compatible theoretical cross section at forward angles. The relatively strongly bound ^{10}Be isotope presents the same behavior as ^{7}Be and ^{9}Be at lower and higher energies, respectively.

C. Boron isotopes

The $^{11,12}\text{B} + {}^9\text{Be}$ scatterings were measured at $E_{\text{lab}}^{^{11}\text{B}} = 31.4$ MeV and at $E_{\text{lab}}^{^{12}\text{B}} = 28.3$ and 34.3 MeV, above the Coulomb barriers at $V_{\text{b}}^{^{11}\text{B}} = 7.28$ and $V_{\text{b}}^{^{12}\text{B}} = 7.57$ MeV. The results can be observed in Figs. 16 and 17 and the final parameters are

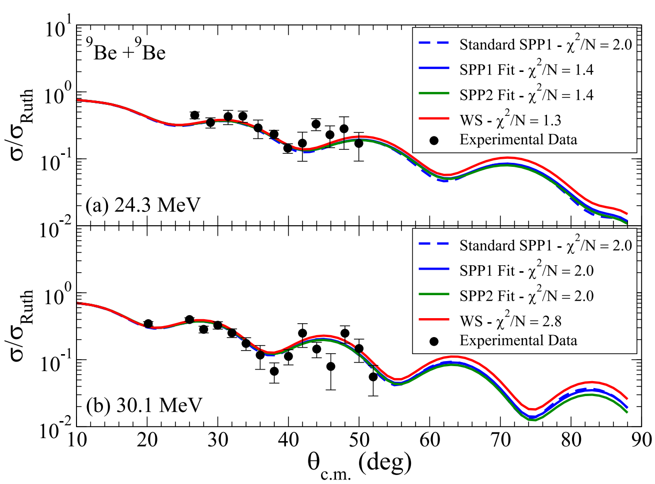

FIG. 13. Angular distributions of the $^9\text{Be} + {}^9\text{Be}$ system at $E_{\text{lab}} =$ 24.3 (a) and 30.1 MeV (b) compared with theoretical results.

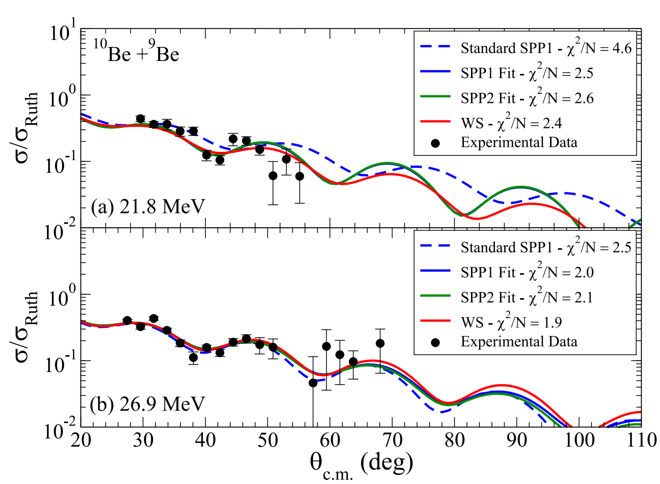

FIG. 14. Angular distributions of the $^{10}\text{Be} + {}^9\text{Be}$ system at $E_{\text{lab}} = 21.8$ (a) and 26.9 MeV (b) compared with theoretical results.

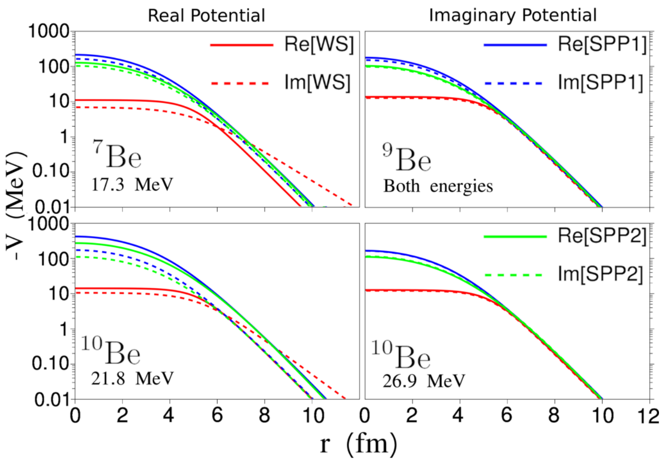

FIG. 15. Optical potentials obtained for beryllium systems.

given in Table IV. The $^{11}B + {}^9Be$ data are well reproduced by the WS potential with no variation in geometry parameters and standard normalizations in SPP1. Again, SPP2 required minor values to be in agreement with the data.

For the ^{12}B projectile, the optical model calculations provided a general potential and an agreement with the experimental data using standard geometry parameters. The standard São Paulo potentials are in good agreement with the $^{12}B + {}^9Be$ experimental angular distributions, reproducing the oscillations rather well. Although $^{12}B + {}^9Be$ is a very neutron rich system, no long range imaginary potential was necessary to reproduce the data.

The potential plot for the $^{11,12}B$ projectiles is shown in Fig. 18. As can be observed, both boron isotopes present similar potentials and show the same peripheral behavior. Again, the angular range of the experimental points provides information about the peripheral region, and more data at backward angles are needed to analyze the internal potential.

1. The ^{8}**B** + ^{9}**Be** *scattering*

The $^8B + {}^9Be$ angular distribution at $E_{lab}^{^8B} = 23.7$ MeV deserves a separate analysis. The ^8B projectile is a very exotic *p*-rich nucleus which has a strong cluster structure formed by a loosely bound proton ($S_p = 0.136$ MeV) and a ^7Be radioactive core. The Coulomb barrier for the $^8B + {}^9Be$ system lies at $V_b^{^8B} = 6.43$ MeV. The experimental data can be observed in Fig. 19 and the final search parameters are presented in Table IV. Despite the limited angular range of the $^8B + {}^9Be$ measurements, a clear oscillation is observed in the data, which is not reproduced by the usual standard São Paulo potential. In contrast to the previous systems, the ^8B experimental angular distribution required very unusual optical potentials to reproduce the data. An unrealistic normalization in the real part of both versions of the São Paulo potential was obtained, indicating that the double folding potential geometry had to be changed for this system. Thus, we decided to focus the subsequent analysis only on the pure Woods-Saxon potential, where the geometry shape can be changed. A good fit was obtained with geometric parameters close to the standard values in the imaginary part; however, a large diffuseness in the real part was necessary, indicating the unusual shape of the $^8B + {}^9Be$ potential.

Figure 20 presents the radial dependence of the best fit obtained with the WS potential. The top image shows the components of the WS potential, and, as one can see, the real part interacts at larger distances than the imaginary one. In the bottom image we plot the $W(r)/V(r)$ ratio as a function of the radial distance, where we see that the ratio is approximately constant in the nuclear interior, presenting a maximum around $r = 4$ fm and quickly dropping down to negligible values at larger distances. This image also shows a comparison between

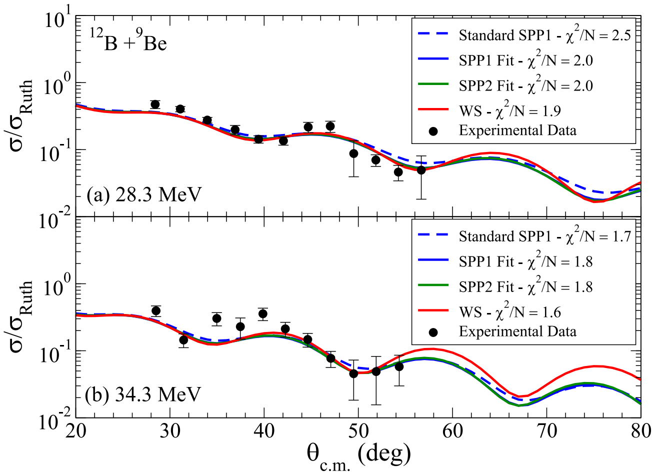

FIG. 17. Angular distributions of the $^{12}B + {}^9Be$ system at $E_{lab} =$ 28.3 (a) and 34.3 MeV (b) compared with theoretical results.

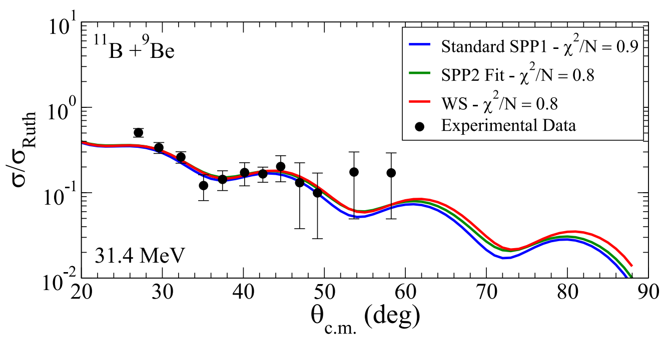

FIG. 16. Angular distributions of the $^{11}B + {}^9Be$ system at $E_{lab} =$ 31.4 MeV compared with theoretical results.

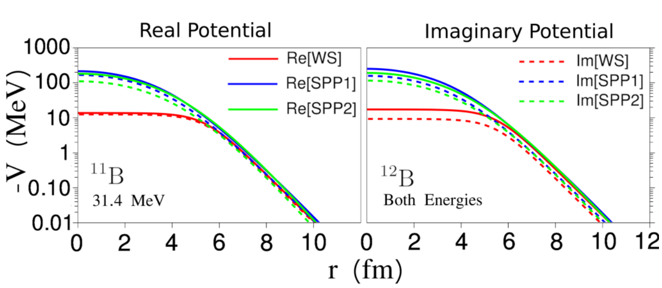

FIG. 18. Optical potentials obtained for boron systems.

TABLE IV. Optical model parameters for the boron systems, obtained by a systematic search (the parameters without uncertainties were kept fixed during the search).

Projectile	E_{lab} (MeV)	Woods-Saxon V (MeV)	r_0 (fm)	a_0 (fm)	W (MeV)	r_i (fm)	a_i (fm)	χ^2/N	SPP1 N_{Re}	N_{Im}	χ^2/N Stand.	χ^2/N Varied	SPP2 N_{Re}	N_{Im}	χ^2/N Varied
^{8}B	23.7	18.2(1)	1.32(6)	1.3(1)	16.8(1)	1.27(1)	0.8(1)	0.9	36.9(3)	0.370(4)	62.8	2.6	15.2(2)	0.102(3)	1.9
^{11}B	31.4	13.7(2)	1.25	0.65	12.5(2)	1.25	0.65	0.8	1.0	0.78	0.9		0.68(1)	0.59(2)	0.8
^{12}B	28.3	17.3(2)	1.25	0.65	9.3(2)	1.25	0.65	1.9	1.0	0.78	2.5		0.81(1)	0.49(2)	2.0
	34.3	17.3(2)	1.25	0.65	9.3(2)	1.25	0.65	1.6	1.0	0.78	1.7		0.81(1)	0.49(2)	1.8

the $W(r)/V(r)$ ratio for the fitted Woods-Saxon potential ($a_0 = 1.3$ fm) and the same ratio with smaller real nuclear diffuseness ($a_0 = 0.8$ fm) (dashed-dotted line), indicating the dominance of the real potential ($V \gg W$) for $r > 6$ fm in the former case. This result can be understood as a peripheral transparency where refraction is still present but with a very small absorption.

The Fig. 21 shows the near-far scattering amplitude decomposition for the ^{8}B + ^{9}Be system. The near side is clearly dominant at very forward angles, where no data are available. At intermediate angles, where data are available, the far side becomes comparable to the near side in magnitude, and the near-far interference produces the observed oscillations. The near side continues to drop as the far side becomes dominant for backward angles, where only one experimental point is available at 57°. The near-far interference and far-side dominance for angles above 40° is an effect of the long range attractive potential associated with a small peripheral absorption. Although an analogous behavior has already been predicted [37] and observed in neutron halo nuclei, such as in the ^{6}He + ^{12}C [38–40] and ^{11}Li + ^{12}C [41] scattering, this pattern had never been observed in proton halo cases.

Interesting clues about the structure features of the ^{8}B isotope can be obtained by a comparison with its mirror nucleus ^{8}Li. For the ^{8}Li + ^{9}Be scattering, at both energies measured in this work, the near-far interference is not as important as in the ^{8}B + ^{9}Be case (Fig. 22). At the lower energy (15.4 MeV) the near-side amplitude (dashed-dotted line) seems to dominate over the far-side amplitude (dashed line), which is at least one order of magnitude smaller in all of the angular range. For the higher energy the far-side amplitude becomes more expressive and presents the same order of magnitude as that of the near side at backward angles ($\theta_{\text{c.m.}} > 60°$). The obtained Woods-Saxon parameters for the ^{8}B and ^{8}Li nuclei have similar imaginary parameters, but very different real ones.

A larger total reaction cross section (see Table V) was obtained for the potentials that reproduce the ^{8}B + ^{9}Be data in comparison to the other systems measured here. The observed effect seems to be more of a refractive one rather than an absorptive one in the nuclear surface; however this large total reaction cross section indicates that the absorption was very strong in the nuclear interior (see Fig. 20 bottom). Reasonable fits could also be obtained using strongly absorptive WS potentials; however, the extracted total reaction cross sections were unrealistically large to be taken as a physically acceptable result.

IV. TOTAL REACTION CROSS SECTIONS

The total reaction cross sections (TRCS) obtained from the optical model analysis are given in Table V. The average values are presented in the last column and were calculated by averaging the three values weighted by the inverse of the χ^2/N of the fits. The uncertainties are given by the standard deviations. In order to compare these quantities for different systems and energies, it is necessary to rescale the TRCS in

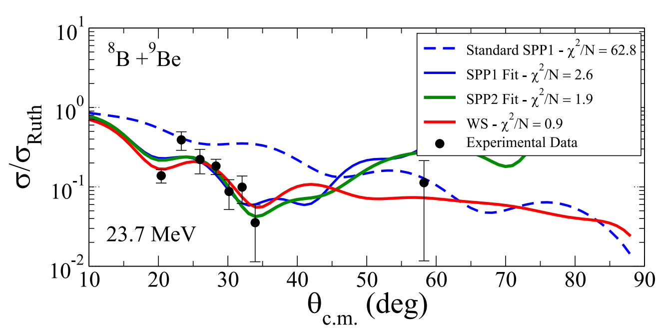

FIG. 19. Angular distributions of the ^{8}B + ^{9}Be system at E_{lab} = 23.7 MeV compared with theoretical results.

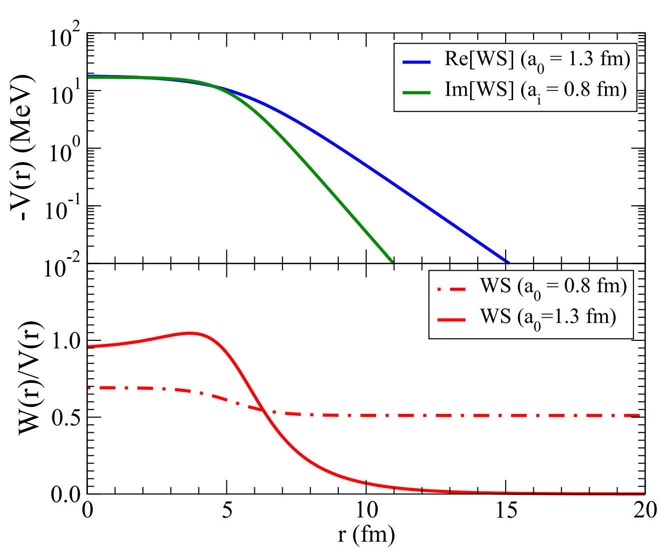

FIG. 20. Woods-Saxon potentials obtained for the ^{8}B + ^{9}Be system.

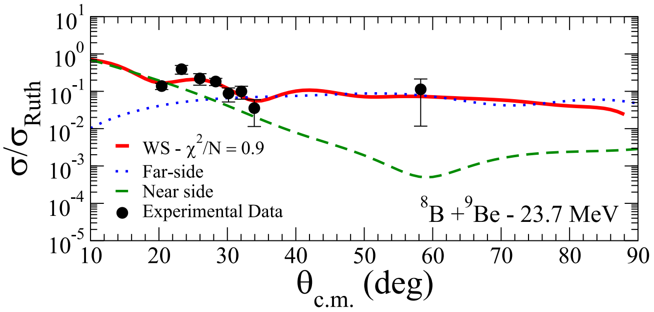

FIG. 21. Near-far decomposition of the $^8B + ^9Be$ system.

order to remove the trivial geometric effects due to different nuclear sizes and energies with respect to the Coulomb barrier. Considering the well know geometric formula and only energies above the Coulomb barrier, the reduction method consist in defining the following quantities: $\sigma_{red} = \bar{\sigma}_R/\pi R_B^2$ and $E_{red} = E/V_B$ for each system. Here R_B and V_B are the Coulomb barrier radius and height, respectively, and are calculated by the realistic values computed by the formulas from Ref. [35].

A comparison between the obtained values and the other data, compiled by Ref. [4], can be observed in Fig. 23. Here it is possible to define three different regions by the nucleus kind: tightly bound (green contour), weakly bound or unstable (blue contour), and halo (red contour). Light systems still lack more accurate data to separate the weakly bound and unstable region and populate the tightly bound systems at $E_{red} \geqslant 8$. The obtained TRCS for the $^{7,10}Be$ nuclei are slightly above the predictions, but other high values were also obtained in other works [4]. Finally, a systematic increase of the reduced total reaction cross section is observed for the halo systems and especially for the $^8B + ^9Be$ system measured in this work, which is a very exotic system due to the low binding energy of the projectile and the target.

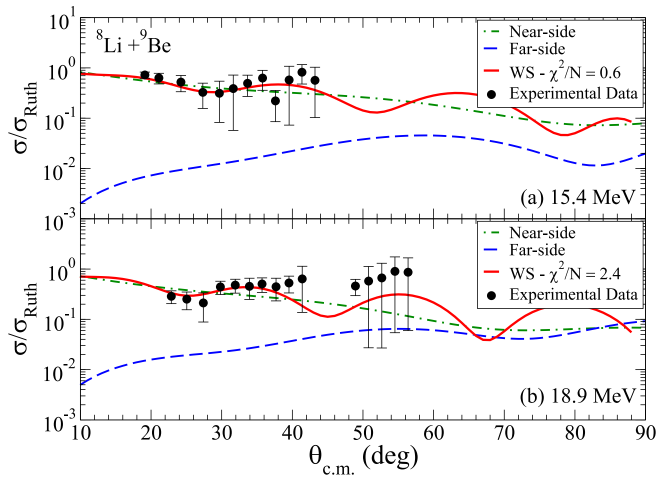

FIG. 22. Near-far decomposition for the WS potential of $^8Li + ^9Be$ system, showing the near-side (green dashed-dotted line) and far-side (blue dashed line) cross sections.

TABLE V. Total reaction cross sections.

System	E_{lab} (MeV)	WS	SPP1	SPP2	$\bar{\sigma}_R$ (mb)
	11.2	1079	1104	1134	1107(16)
$^6Li + ^9Be$	21.1	1151	1185	1217	1176(19)
	25.7	1144	1183	1216	1183(21)
	17.7	1271	1269	1289	1276(6)
$^7Li + ^9Be$	21.9	1303	1301	1320	1307(6)
	15.4	1376	1207	1224	1257(54)
$^8Li + ^9Be$	18.9	1516	1293	1323	1353(70)
$^7Be + ^9Be$	17.3	1445	1281	1286	1332(54)
	24.3	1311	1309	1313	1311(1)
$^9Be + ^9Be$	30.1	1344	1341	1346	1344(1)
	21.8	1604	1469	1462	1513(46)
$^{10}Be + ^9Be$	26.4	1343	1350	1355	1349(3)
$^8B + ^9Be$	23.7	1773	1982	1404	1717(169)
$^{11}B + ^9Be$	31.4	1331	1340	1328	1333(4)
	28.3	1329	1370	1348	1342(9)
$^{12}B + ^9Be$	34.3	1376	1422	1502	1390(10)

V. CC, CDCC, AND CRC

The strong cluster structure present in most of the projectiles studied here suggests that the coupling to the inelastic excitation, projectile breakup, and transfer reaction channels could have an effect on the angular distributions. In addition, the low lying bound excited states of some projectiles associated with our limited energy resolution require an estimation of the effect of an inelastic contamination in the elastic scattering peaks (quasielastic scattering). All these effects were investigated by the coupled channels method: CC calculations for the inelastic scattering, CDCC for the projectile breakup, and CRC for stripping reactions. The calculations were performed using the program FRESCO [30] and the cluster model was used to describe the projectile-target interaction:

$$V_{p,t} = \langle \phi_p | V_{c-t} + V_{v-t} | \phi_t \rangle , \quad (5)$$

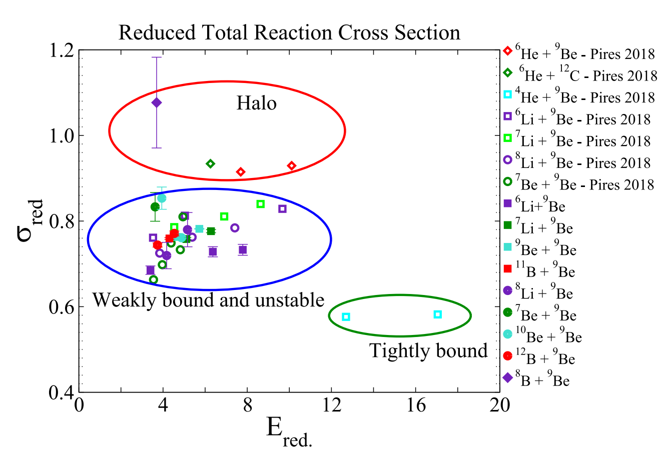

FIG. 23. Reduced total reaction cross section for stable, unstable, and halo projectiles on light targets. Comparison of the present data and obtained from Pires (2018) [4].

TABLE VI. Cluster configurations for each projectile, core-valence binding energies and the energy of the low lying excited state.

Cluster (c + v)	BU (MeV)	E_x (MeV)
^{6}Li $\rightarrow$ α + d	1.473	2.186
^{7}Li $\rightarrow$ α + t	2.467	0.477
^{8}Li $\rightarrow$ ^{7}Li + n	2.032	0.980
^{7}Be $\rightarrow$ ^{4}He + ^{3}He	1.587	0.429
^{9}Be $\rightarrow$ $\alpha + \alpha$ + n	1.664	1.684
^{10}Be $\rightarrow$ ^{9}Be + n	6.812	3.367
^{8}B $\rightarrow$ ^{7}Be + p	0.136	0.769
^{11}B $\rightarrow$ ^{7}Li + α	8.664	2.124
^{12}B $\rightarrow$ ^{11}B + n	3.369	0.953

where $\phi_{p,t}$ is the projectile-target wave function, and $V_{c\text{-}t}$ and $V_{v\text{-}t}$ are the complex core-target and valence-target interactions, respectively. All breakup (BU) configurations are presented in Table VI. In the cases of CC and CDCC calculations, the core-target optical potentials were obtained from the standard São Paulo potential or from other measurements involving light systems (^{7}Be + ^{9}Be [42] or ^{4}He + ^{9}Be [43]). The core-valence and valence-target interactions were described using the Perey-Perey optical model compilation [44]. For CRC calculations, the bare and core-residual potentials must be explicitly included and will be further explained. Furthermore, it was considered that all excitation, breakup, or transfer processes come from the projectile ground state. In most systems, a very weak effect on the elastic cross section was noted due to coupling with reaction channels; therefore, to summarize all the results only the most relevant ones will be present. In all cases, the core remains in the ground state after the reaction.

A. CC calculations for the inelastic excitation

Primarily, we will present the CC results for ^{7,8}Li, ^{7}Be and ^{12}B, due to the fact that the low lying excitation energies of these isotopes are smaller than our beam resolution. These calculations are performed using the single-particle model for the excited states and no collective excitation model was included. All states below the breakup threshold (bound states) were included [45].

The results for the ^{7,8}Li + ^{9}Be, ^{7}Be + ^{9}Be, and ^{12}B + ^{9}Be systems are shown in Figs. 24–27. As one can observe, the theoretical results of pure elastic scattering (dashed green line) and the sum over ground and all included excited states (red line) have almost the same behavior in the experimental data region. Furthermore, the inelastic cross sections (dotted line) are at least one order of magnitude smaller than elastic ones in that angular range. These facts indicate that elastic scattering is dominant and the effect of projectile excitation would be very small in this angular region. Its also notable that the coupling of inelastic channels does not have a remarkable effect since no significant differences can be noted between the bare (dashed blue line) and coupling calculations (red line). This negligible effect can be interpreted by the high scattering energy when compared with the barrier height, that minimizes the Coulomb excitation.

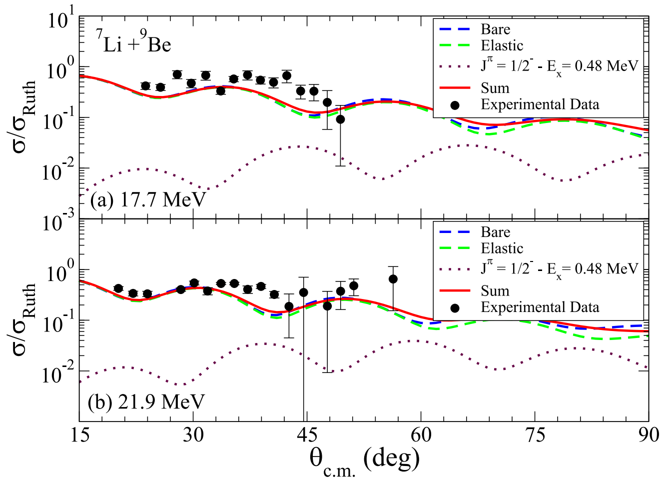

FIG. 24. CC calculations of the ^{7}Li + ^{9}Be system at $E_{\text{lab}} = 17.7$ (a) and 21.9 MeV (b) compared with experimental data.

B. CDCC for the breakup

For the exotic ^{8}B case, the radioactive core (^{7}Be) is also a weakly bound isotope and, due to this fact, we explore the sensitivity of the CDCC calculations for different core-target interactions. Three optical potentials were used for the ^{7}Be + ^{9}Be system: one obtained in this work and two in Refs. [5,42]. No core (^{7}Be) excitation was considered in the CDCC procedure and the ejected proton's total angular momentum has been set up to the maximum value $l = 3$ (f wave), in order to ensure the convergence of the calculations. The Fig. 28 shows the comparison between the data and CDCC results, and, as one can see, the coupling with the continuum slightly attenuates the oscillations amplitude; however, it does not reproduce the experimental data.

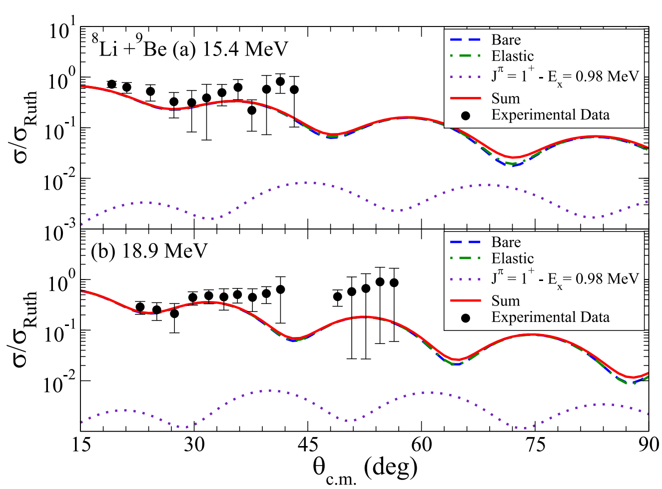

FIG. 25. CC calculations of the ^{8}Li + ^{9}Be system at $E_{\text{lab}} = 15.4$ (a) and 18.9 MeV (b) compared with experimental data.

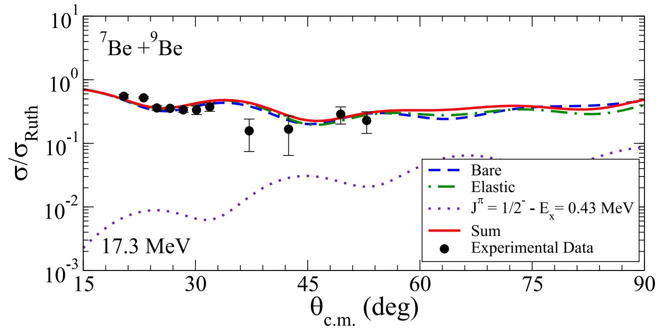

FIG. 26. CC calculations of $^7\mathrm{Be} + {}^9\mathrm{Be}$ system at $E_{\mathrm{lab}} = 17.3$ MeV compared with experimental data.

The only system that showed some effect due to the coupling with the breakup channel was $^7\mathrm{Be} + {}^9\mathrm{Be}$. The core (^{4}He) remains in the ground state ($J^\pi = 0^+$) after the reaction and the calculation convergence was achieved when the valence particle total angular momentum was set up to $l = 4$ (g wave). The core-valence ($^4\mathrm{He} + {}^3\mathrm{He}$) binding state was described by a real potential [44], where the depth was varied to reproduce the biding energy. The $^4\mathrm{He} + {}^9\mathrm{Be}$ and $^3\mathrm{He} + {}^9\mathrm{Be}$ optical potentials were obtained from Refs. [46] and [43], respectively. The calculations (see Fig. 29) show a small effect at forward angles followed by a decrease in χ^2/N values for greater angular momenta. However, more data at backward angles are needed to assert that this coupling is relevant to the elastic scattering process.

C. CRC for stripping

Finally, we performed CRC calculations to investigate the effect of the transfer (stripping) channel coupling with the elastic scattering data. Only the analysis for the $^8\mathrm{B} + {}^9\mathrm{Be}$ system will be presented. The choice of the bare potential plays a critical role in this case and we used three types of potentials. The first potential is SPP1 potential [see Fig. 30(a)] and the second is SPP2 [see Fig. 30(b)], both with $N_{\mathrm{Re}} = 1.0$ and $N_{\mathrm{Im}} = 0.6$. This imaginary normalization was already successfully used in transfer reaction calculations [5,47]. The third potential is a long range WS potential [Fig. 30(c)], with the parameters obtained in this work and a rescaling of the imaginary depth to avoid doublecounting of the considered reaction channel (similarly to that performed in the São Paulo potential case). Again, we apply three potentials to the $^7\mathrm{Be} + {}^9\mathrm{Be}$ interaction (obtained in this work and in Refs. [5,42]). The valence-target ($p + {}^9\mathrm{Be}$) binding potential was obtained from Ref. [44], with a variation of the real depth to reproduce the BU energy. For the core-residual potential we used SPP1 with the standard normalizations. The residual nuclei (^{10}B) spectroscopic factors were experimentally measured

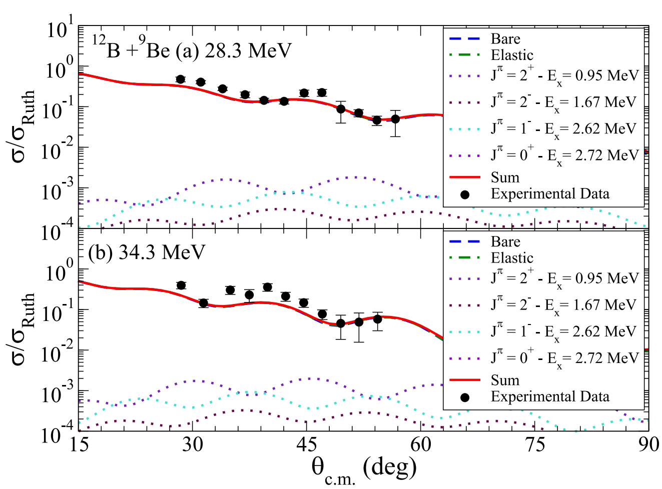

FIG. 27. CC calculations of the $^{12}\mathrm{B} + {}^9\mathrm{Be}$ system at $E_{\mathrm{lab}} = 28.3$ (a) and 34.3 MeV (b) compared with experimental data.

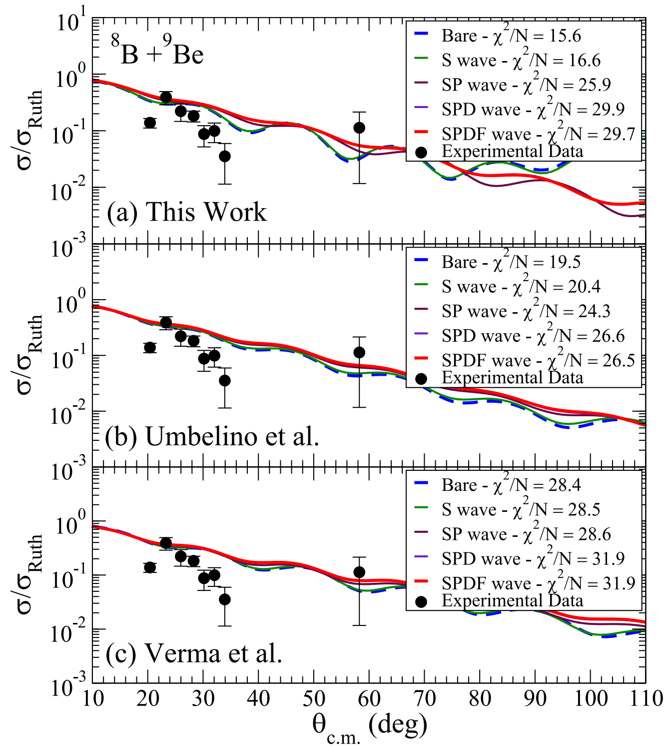

FIG. 28. CDCC calculations of the $^8\mathrm{B} + {}^9\mathrm{Be}$ system at $E_{\mathrm{lab}} = 23.7$ MeV compared with experimental data. The figures identifications refer to different $^7\mathrm{Be} + {}^9\mathrm{Be}$ interaction potentials (see the text for more details).

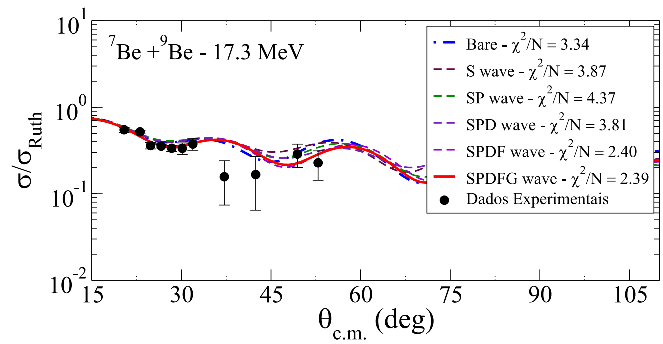

FIG. 29. CDCC calculations of the $^7\mathrm{Be} + {}^9\mathrm{Be}$ system at $E_{\mathrm{lab}} = 17.3$ MeV compared with experimental data.

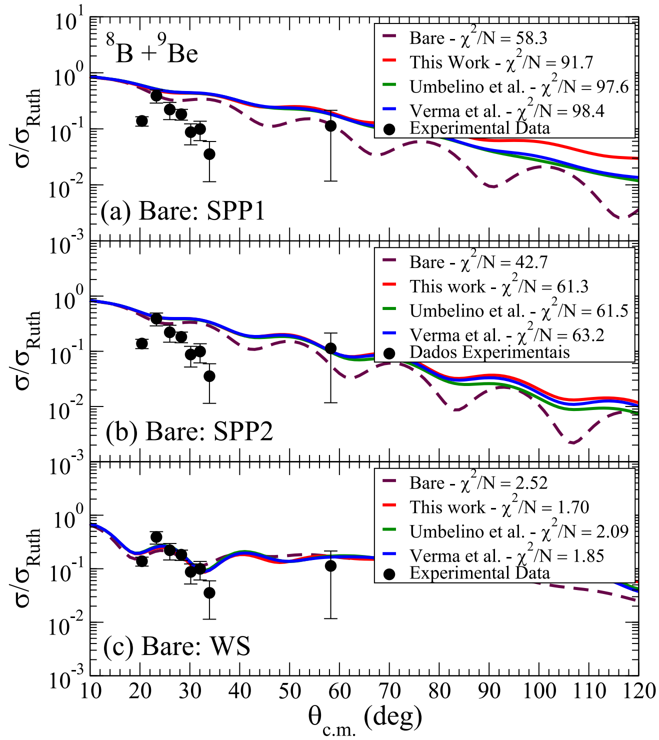

FIG. 30. CRC calculations of the $^8B + ^9Be$ system at $E_{lab} = 23.7$ MeV compared with experimental data. The figures identifications refer to different $^7Be + ^9Be$ interaction potentials (see the text for more details).

using the $^9Be(d, n)\,^{10}B$ reaction [48–51] and compiled for this calculation. As one can see (Fig. 30), the different $^7Be + ^9Be$ used potentials did not result in relevant differences and only the long range WS bare potential showed some agreement with the data. However, the theoretical cross section without any coupling (bare) already reproduced the oscillation pattern, indicating that the refractive behavior is caused by a static potential of this system. The small decrease in the χ^2/N values leads to the possibility of a significant coupling between the stripping and elastic channels, but only more backward data can prove this.

These coupled channels method calculations (CC, CDCC, and CRC) show us that the effects of couplings of the inelastic, breakup, and transfer channels in the elastic scattering are not as relevant as those found in heavier systems [10,25,52,53] in the angular region of the experimental data measured in this work.

VI. SUMMARY AND CONCLUSIONS

Sixteen quasielastic angular distributions of weakly bound, unstable and exotic projectiles (^{6,7,8}Li, ^{7,9,10}Be, and ^{8,11,12}B) on a ^{9}Be target have been measured using a cocktail secondary beam produced by the RIBRAS facility, at energies ranging from 4 up to 7 times the Coulomb barriers. The experimental angular distributions present an exponential fall with oscillations in the σ/σ_{Ruth} ratio typical of near-far interference. All the angular distributions have been optical model analyzed using the double folding São Paulo potential and a Woods-Saxon parametrization adjusted to best fit the data. Most of the angular distributions present oscillations which are well reproduced by the standard São Paulo or Woods-Saxon potentials with standard geometries. A comparison between the different potentials shows that, for most of the systems, the tail of the potentials above $r \geqslant 5$ fm is well determined, indicating that this is the region of sensitivity of the data. The tails of the real and imaginary potentials seem to be the same for WS and SPP except for the ^{8}Li, ^{7}Be, and ^{10}Be projectiles, for which the WS potential apparently has a larger diffuseness, crossing the SPP tail at $r \approx 6.5$ fm. For inner regions ($r \leqslant 5$ fm) the potentials differ considerably, the SPP being much deeper.

For the $^8B + ^9Be$ system the potentials with usual geometries were not to able to reproduce the angular distribution. For this system, the standard São Paulo potential predicts differential cross sections considerably above the data and an unrealistically large real normalization is necessary to improve the fit, in both versions (SPP1 and SPP2). Better results were obtained with the Woods-Saxon potential, and a long range real potential seems to be necessary to reproduce the data. This real long range tail contrasts with the observations seen so far for scattering induced by exotic projectiles on heavy targets, where a long range imaginary potential, rather than a real one, was observed. However, given the limited angular range of the $^8B + ^9Be$ elastic scattering data no definite conclusion is possible here.

Total reaction cross sections have been obtained from the optical model calculations for all systems. The cross sections have been reduced and compared in the same plot for different systems. An increase in the total reaction from tightly to weakly bound and to the exotic ^{8}B projectile, which presents the highest cross section, was observed.

The CC, CRC, and CDCC calculations were performed for all data considering the projectile excitation, coupling to transfer reactions (stripping), and coupling to the projectile breakup, and no significant effect in the angular range of the present data was observed. In particular for the $^8B + ^9Be$ system, the CDCC and CRC calculations considering $p + ^7Be$ do not seem to give an explanation for the observed anomaly in the $^8B + ^9Be$ optical model potential.

ACKNOWLEDGMENTS

This work has been supported by the Coordenação de Aperfeiçoamento de Pessoal de Nível Superior, CAPES (Brazil). A part of the work was developed under the project of the Instituto Nacional de Ciência e Tecnologia: Físíca Nuclear e Aplicações, INCT-FNA (Brazil), Proc. No. 464898/2014-5, Conselho Nacional de Desenvolvimento Científico e Tecnológico, CNPq (Brazil), No. 405138/2021-0, Fundação de Amparo à Pesquisa do Estado de São Paulo, FAPESP (Brazil), Contracts No. 2019/02759-0, No. 2019/07767-1, No. 2016/17612-7, No. 2013/22100-7, and No. 2019/05769-7.

[1] E. A. Benjamim, A. Lépine-Szily, D. R. Mendes Jr., R. Lichtenthäler, V. Guimarães, P. R. S. Gomes *et al.*, Elastic scattering and total reaction cross section for the ^{6}He + ^{27}Al system, Phys. Lett. B **647**, 30 (2007).
[2] K. C. C. Pires, R. Lichtenthäler, A. Lépine-Szily, V. Guimarães, P. N. de Faria, A. Barioni *et al.*, Experimental study of ^{6}He + ^{9}Be elastic scattering at low energies, Phys. Rev. C **83**, 064603 (2011).
[3] K. C. C. Pires, R. Lichtenthäler, A. Lépine-Szily, and V. Morcelle, Total reaction cross section for the ^{6}He + ^{9}Be system, Phys. Rev. C **90**, 027605 (2014).
[4] K. C. C. Pires, S. Appannababu, R. Lichtenthäler, and O. C. B. Santos, New method to calculate the nuclear radius from low energy fusion and total reaction cross sections, Phys. Rev. C **98**, 014614 (2018).
[5] U. Umbelino, K. C. C. Pires, R. Lichtenthäler, V. Scarduelli, G. A. Scotton, A. Lépine-Szily *et al.*, Two-neutron transfer in ^{7}Be + ^{9}Be collisions, Phys. Rev. C **99**, 064617 (2019).
[6] N. Keeley *et al.*, Elastic scattering and reactions of light exotic beams, Prog. Part. Nucl. Phys. **63**, 396 (2009).
[7] A. Pakou, E. Stiliaris, D. Pierroutsakou, N. Alamanos, A. Boiano, C. Boiano *et al.*, Fusion cross sections of ^{8}B + ^{28}Si at near-barrier energies, Phys. Rev. C **87**, 014619 (2013).
[8] F. A. Souza, C. Beck, N. Carlin, N. Keeley, R. Liguori Neto, M. M. de Moura *et al.*, Reaction mechanisms in the ^{6}Li + ^{59}Co system, Nucl. Phys. A **821**, 36 (2009).
[9] A. Pakou, N. Alamanos, A. Gillibert, M. Kokkoris, S. Kossionides, A. Lagoyannis *et al.*, α-Particle Production in the Reaction ^{6}Li + ^{28}Si at Near-Barrier Energies, Phys. Rev. Lett. **90**, 202701 (2003).
[10] P. N. de Faria, R. Lichtenthäler, K. C. C. Pires, A. M. Moro, A. Lépine-Szily, V. Guimarães *et al.*, Elastic scattering and total reaction cross section of ^{6}He + ^{120}Sn, Phys. Rev. C **81**, 044605 (2010).
[11] S. Appannababu, R. Lichtenthäler, M. A. G. Alvarez, M. Rodríguez-Gallardo, A. Lépine-Szily, K. C. C. Pires *et al.*, Two-neutron transfer in the ^{6}He + ^{120}Sn reaction, Phys. Rev. C **99**, 014601 (2019).
[12] V. Pesudo, M. J. G. Borge, A. M. Moro, J. A. Lay, E. Nácher, J. Gómez-Camacho *et al.*, Scattering of the Halo Nucleus ^{11}Be on ^{197}Au at Energies around the Coulomb Barrier, Phys. Rev. Lett. **118**, 152502 (2017).
[13] M. Cubero, J. P. Fernández-García, M. Rodríguez-Gallardo, L. Acosta, M. Alcorta, M. A. G. Alvarez *et al.*, Do Halo Nuclei Follow Rutherford Elastic Scattering at Energies Below the Barrier? The Case of ^{11}Li, Phys. Rev. Lett. **109**, 262701 (2012).
[14] A. Di Pietro, G. Randisi, V. Scuderi, L. Acosta, F. Amorini, M. J. G. Borge *et al.*, Elastic Scattering and Reaction Mechanisms of the Halo Nucleus ^{11}Be around the Coulomb Barrier, Phys. Rev. Lett. **105**, 022701 (2010).
[15] O. R. Kakuee, J. Rahighi, A. M. Sánchez-Benítez, M. V. Andrés, S. Cherubini, T. Davinson *et al.*, Elastic scattering of the halo nucleus ^{6}He from ^{208}Pb above the Coulomb barrier, Nucl. Phys. A **728**, 339 (2003).
[16] A. Lépine-Szily, R. Lichtenthäler, and V. Guimarães, The Radioactive Ion Beams in Brazil (RIBRAS) facility, Eur. Phys. J. A **50**, 128 (2014).
[17] J. J. Kolata, V. Guimarães, and E. F. Aguilera, Elastic scattering, fusion, and breakup of light exotic nuclei, Eur. Phys. J. A **52**, 136477 (2016).
[18] F. F. Duan, Y. Y. Yang, K. Wang, A. M. Moro, V. Guimarães, D. Y. Pang *et al.*, Scattering of the halo nucleus ^{11}Be from a lead target at 3.5 times the Coulomb barrier energy, Phys. Lett. B **811**, 135942 (2020).
[19] R. Spartà, A. Di Pietro, P. Figuera, O. Tengblad, A. M. Moro, I. Martel *et al.*, Probing proton halo effects in the ^{8}B + ^{64}Zn collision around the Coulomb barrier, Phys. Lett. B **820**, 136477 (2021).
[20] Y. Y. Yang, J. S. Wang, Q. Wang, D. Pang, J. B. Ma, M. R. Huang *et al.*, Elastic scattering of the proton drip-line nucleus ^{8}B off a $^{\rm nat}$Pb target at 170.3 MeV, Phys. Rev. C **87**, 044613 (2013).
[21] P. Fröbrich and R. Lipperheide, *Theory of Nuclear Reactions* (Clarendon, Oxford, 1996), p. 37.
[22] P. R. S. Gomes, I. Padron, M. Rodríguez, G. Martí, R. Anjos, J. Lubian *et al.*, Fusion, reaction and break-up cross sections of weakly bound projectiles on ^{64}Zn, Phys. Lett. B **601**, 20 (2004).
[23] P. N. de Faria, R. Lichtenthäler, K. C. C. Pires, A. M. Moro, A. Lépine-Szily, V. Guimarães *et al.*, α-particle production in ^{6}He + ^{120}Sn collisions, Phys. Rev. C **82**, 034602 (2010).
[24] V. Morcelle, R. Lichtenthäler, R. Linares, M. C. Morais, V. Guimarães, A. Lépine-Szily *et al.*, Elastic scattering and total reaction cross section for the ^{7}Be + ^{27}Al system at near-barrier energies, Phys. Rev. C **89**, 044611 (2014).
[25] V. Morcelle, R. Lichtenthäler, A. Lépine-Szily, V. Guimarães, K. C. C. Pires, J. Lubian *et al.*, ^{8}B + ^{27}Al scattering at low energies, Phys. Rev. C **95**, 014615 (2017).
[26] R. Lichtenthäler, A. Lépine-Szily, V. Guimarães, C. Perego, V. Placco, O. Camargo, Jr. *et al.*, Radioactive Ion beams in Brazil (RIBRAS), Eur. Phys. J. A **25**, 733 (2005).
[27] R. Lichtenthäler, M. A. G. Alvarez, A. Lépine-Szily, S. Appannababu, K. C. C. Pires, U. U. da Silva *et al.*, RIBRAS: The facility for exotic nuclei in Brazil, Few Body Syst. **57**, 157 (2016).
[28] R. Lichtenthäler, O. C. B. Santos, A. Serra, U. Umbelino, K. C. C. Pires, J. R. B. Oliveira *et al.*, Experiments with A = 6–8 exotic beams in RIBRAS, Eur. Phys. J. A **57**, 92 (2021).
[29] R. Lichtenthäler, RIBRAS code (unpublished).
[30] I. J. Thompson, Coupled reaction channels calculations in nuclear physics, Comput. Phys. Rep. **7**, 167 (1988).
[31] L. C. Chamon, B. V. Carlson, L. R. Gasques, D. Pereira, C. De Conti, M. A. G. Alvarez *et al.*, Toward a global description of the nucleus-nucleus interaction, Phys. Rev. C **66**, 014610 (2002).
[32] M. A. G. Alvarez, L. C. Chamon, M. S. Hussein, D. Pereira, L. R. Gasques, E. S. Rossi *et al.*, A parameter-free optical potential for the heavy-ion elastic scattering process, Nucl. Phys. A **723**, 93 (2003).
[33] L. C. Chamon, B. Carlson, and L. Gasques, São Paulo potential version 2 (SPP2) and Brazilian nuclear potential (BNP), Comput. Phys. Commun. **267**, 108061 (2021).
[34] Wolfram Research, Inc., Mathematica, Version 13.1, 2022, https://www.wolfram.com/mathematica.
[35] A. S. Freitas, L. Marques, X. X. Zhang, M. A. Luzio, P. Guillaumon, R. P. Condori *et al.*, Woods-Saxon equivalent to a double folding potential, Braz. J. Phys. **46**, 120 (2016).
[36] G. Igo, Optical Model Potential at the Nuclear Surface for the Elastic Scattering of Alpha Particles, Phys. Rev. Lett. **1**, 72 (1958).

[37] G. R. Satchler, K. W. Mcvoy, and M. Hussein, Exploratory studies of the elastic scattering of ^{11}Li + ^{12}C, Nucl. Phys. A **522**, 621 (1991).

[38] M. Milin, S. Cherubini, T. Davinson, A. D. Pietro, P. Figuera, D. Miljanić *et al.*, The ^{6}He scattering and reactions on ^{12}C and cluster states of ^{14}C, Nucl. Phys. A **730**, 285 (2004).

[39] F. Michel and S. Ohkubo, Airy minima in the scattering of weakly bound light heavy ions, Phys. Rev. C **72**, 054601 (2005).

[40] V. Lapoux, N. Alamanos, F. Auger, V. Fékou-Youmbi, A. Gillibert, F. Marie *et al.*, Coupling effects in the elastic scattering of ^{6}He on ^{12}C, Phys. Rev. C **66**, 034608 (2002).

[41] J. J. Kolata, M. Zahar, R. Smith, K. Lamkin, M. Belbot, R. Tighe *et al.*, Quasielastic Scattering of ^{11}Li and ^{11}C from ^{12}C at 60 MeV/nucleon, Phys. Rev. Lett. **69**, 2631 (1992).

[42] S. Verma, J. J. Das, A. Jhingan, K. Kalita, S. Barua, K. S. Golda *et al.*, Interaction of loosely bound radioactive ^{7}Be and stable ^{7}Li with ^{9}Be, Eur. Phys. J. A **44**, 385 (2010).

[43] R. B. Taylor, N. R. Fletcher, and R. H. Davis, Elastic scattering of 4–20 MeV alpha particles by ^{9}Be, Nucl. Phys. **65**, 318 (1965).

[44] C. M. Perey and F. G. Perey, Compilation of phenomenological optical-model parameters 1954–1975, At. Data Nucl. Data Tables **17**, 1 (1976).

[45] Brookhaven National Laboratory, National Nuclear Data Center, https://www.nndc.bnl.gov/.

[46] J. Y. Park, J. Duggan, P. Miller, M. Duncan, and R. Dangle, Elastic scattering of ^{3}He particles by ^{9}Be and ^{11}B between 4.0 and 18.0 MeV, Nucl. Phys. A **134**, 277 (1969).

[47] D. Pereira, J. Lubian, J. Oliveira, D. de Sousa, and L. Chamon, An imaginary potential with universal normalization for dissipative processes in heavy-ion reactions, Phys. Lett. B **670**, 330 (2009).

[48] Y. S. Park, A. Niiler, and R. A. Lindgren, Spectroscopy of ^{10}B levels from the ^{9}Be$(d,n)^{10}$B reaction, Phys. Rev. C **8**, 1557 (1973).

[49] S. Buccino and A. Smith, Levels in ^{10}B excited by the ^{9}Be(d,n) reaction, Phys. Lett. **19**, 234 (1965).

[50] A. A. Fife, G. Neilson, and W. Dawson, The excited states of ^{10}B, Nucl. Phys. A **91**, 164 (1967).

[51] K. Miura, A. Sato, J. Takamatsu, S. Mori, Y. Takahashi, T. Nakagawa *et al.*, The ^{9}Be(d,n)^{10}B reaction at 25 MeV, Nucl. Phys. A **539**, 441 (1992).

[52] O. C. B. Santos, R. Lichtenthäler, K. C. C. Pires, U. Umbelino, E. O. N. Zevallos, A. L. de Lara *et al.*, Evidence of the effect of strong stripping channels on the dynamics of the ^{8}Li + ^{58}Ni reaction, Phys. Rev. C **103**, 064601 (2021).

[53] V. Morcelle, K. C. C. Pires, M. Rodríguez-Gallardo, R. Lichtenthäler, A. Lépine-Szily, V. Guimarães *et al.*, Four-body effects in the ^{6}He + ^{58}Ni scattering, Phys. Lett. B **732**, 228 (2014).